Design and operation of a tunable MeV-level Compton-scattering-based γ-ray source

D. J. Gibson,* F. Albert, S. G. Anderson, S. M. Betts, M. J. Messerly, H. H. Phan, V. A. Semenov, M. Y. Shverdin, A. M. Tremaine, F. V. Hartemann, C. W. Siders, D. P. McNabb, and C. P. J. Barty

Lawrence Livermore National Laboratory, Livermore , California 94550, USA

(Received 27 October 2009; published 27 July 2010)

A monoenergetic gamma-ray (MEGa-ray) source based on Compton scattering, targeting nuclear physics applications such as nuclear resonance fluorescence, has been constructed and commissioned at Lawrence Livermore National Laboratory. In this paper, the overall architecture of the system, as well as some of the design decisions (such as laser pulse lengths and interaction geometry) made in the development of the source, are discussed. The performances of the two laser systems (one for electron production, one for scattering), the electron photoinjector, and the linear accelerator are also detailed, and initial γ-ray results are presented.

DOI: 10.1103/PhysRevSTAB.13.070703 PACS numbers: 07.85.Fv, 29.20.Ej, 41.75.Ht, 42.60.−v

In the past decade, Compton- or Thomson-scattering systems, in which incoming high-intensity laser photons scatter off a relativistic electron beam, taking some of the electron energy, and emerge as high-energy x-ray or γ-ray photons, have shown promise as a new class of light source, with applications ranging from atomic [1] to nuclear [2–5] to particle physics [6,7]. Such sources could also be valuable in the medical field [8]. These sources provide an easily tunable, narrow bandwidth beam. We refer to such sources as monoenergetic gamma-ray (MEGa-ray) sources. Operating in the few-MeV photon energy range, these MEGa-ray sources, properly designed, can surpass the peak spectral brightness of current synchrotrons by many orders of magnitude due to their favorable energy scaling properties, where the predicted brightness increases with increasing electron beam (and consequently increasing γ-ray) energy [9].

In this paper we present the architecture and initial operational demonstration of such a source, dubbed the ''Thomson-radiated extreme x-ray'' (T-REX) source, designed to demonstrate the potential target end application of nuclear resonance fluorescence (NRF) detection and imaging. Coupling a MEGa-ray source with NRF can allow advances in a variety of fields, from nuclear waste assay to detailed medical imaging. One particular use we have targeted is cargo interrogation. The narrow bandwidth of the source, along with highly penetrating MeV energies, would enable the detection of particular isotopes of interest in cargo containers. This provides a robust screening method that is not susceptible to the false negatives that can result from shielding inside the cargo container [10–12].

Given the limited space and rf power available at the Lawrence Livermore National Laboratory (LLNL) accelerator facility, we designed a machine to demonstrate NRF measurements by exciting the relatively low-energy lines at 478 keV for ^{7}Li and 680 keV for ^{238}U using ~120 MeV electron energies (note that all energies quoted in this paper are kinetic energies) and either 532 or 351 nm laser light. Because this system is designed for probing the nucleus instead of the electronic structure of materials, we refer to the generated radiation as γ rays, regardless of their exact energy.

A block diagram of the complex system is shown in Fig. 1. Two lasers, sharing a common front end architecture, are used: one generates the electron beam and the other is scattered at the interaction point to generate the γ rays. A photoinjection gun and linac accelerate the electrons liberated from the cathode by the first laser. A high-power rf system provides the energy for acceleration and is carefully synchronized to the laser systems to ensure the concurrent arrival of the laser and electron beams at the interaction point where the scattering occurs. Each of these subsystems is described in detail below, along with initial demonstrations of γ-ray production.

I. LASER SYSTEMS

The T-REX source requires two laser systems that are precisely synchronized: one to generate the electron beam at the photocathode (the ''photoinjector drive laser'' or PDL), and one to scatter off the focused electron beam at the end of the linac (the ''interaction laser system'' or ILS). In order to ensure the synchronicity of the two lasers, they are seeded with the same fiber-based oscillator. Both lasers have matching front ends that are all fiber based (collectively, the ''seed laser system'' or SLS), which then feed into the main PDL and ILS systems. A summary of the parameters of the two laser systems are presented in Table I.

A. Seed laser system (SLS)

A passively mode-locked fiber oscillator, based on a design for the National Ignition Facility (NIF) at LLNL

*gibson23@llnl.gov

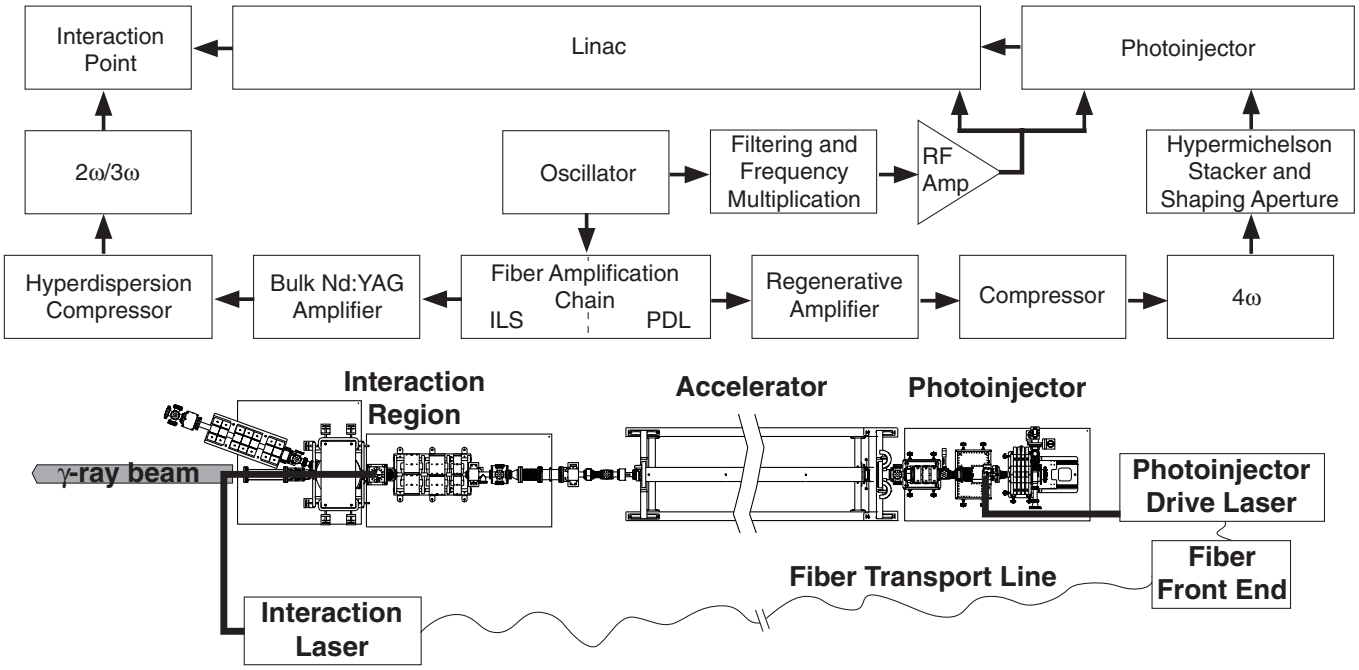

FIG. 1. Top: A block diagram of the T-REX system, showing all the subcomponents described in detail in the text. Bottom: A schematic of the integrated system.

[13], produces 0.4 nJ pulses with a spectral bandwidth that is sufficient for 70 fs FWHM pulses. These pulses are generated at a repetition rate of 40.7785 MHz and have a spectrum centered at 1045 nm (Fig. 3, top). After leaving the oscillator, the pulses are split in amplitude and sent to the PDL and ILS fiber amplifier chains, which are shown schematically in Fig. 2. In the PDL subsystem, a chirped fiber Bragg grating (CFBG) [14] is used as the pulse stretcher. The CFBG narrows the spectrum to 8 nm (Fig. 3, top) and stretches the pulses to 1.5 ns. The loss through the stretcher is 18 dB (6 dB of which results from the mentioned spectral narrowing). The stretched pulses are amplified by a series of three custom-built Yb-doped fiber preamplifiers. The preamplifier fibers have a mode diameter of 6 μm, and each preamp produces roughly 17 dB of gain. Accumulated amplified spontaneous emission (ASE) is stripped between stages in the spectral and time domains; the latter by acousto-optic modulators (AOMs). The AOMs also reduce the pulse repetition rate to roughly 10 kHz in order to keep the average power from the preamplifiers modest as the pulse energy increases. This 10 kHz rate is high enough to prevent the gain from growing to the point where spontaneous lasing can occur.

After the final fiber preamp, the pulse energy is roughly 1 μJ. The PDL's final fiber preamplifier is followed by a fiber amplifier based on a single-mode, single-polarization fiber having a mode diameter of 29 μm (Crystal Fibre PZ-41). This amplifier boosts the energy to 50 μJ at 10 kHz. Figure 3 compares the spectra directly from the oscillator, after the CFBG, after the final amplifier, and after the regenerative amplifier (discussed below). The gain of the Yb tilts the fiber amplifier spectrum.

TABLE I. Summary of SLS, PDL, and ILS parameters after amplification and compression.

Parameter	SLS	PDL	ILS
System type	Yb fiber	Nd:glass	Nd:YAG
Stretched pulse length	1.5 and 5 ns	1.5 ns	5 ns
Repetition rate	10 kHz	10 Hz	10 Hz
Amplified energy	30 μJ	1.5 mJ	700 mJ
Center wavelength	1053 and 1064 nm	1053 nm	1064 nm
Bandwidth (FWHM)	8 and 0.8 nm	4 nm	0.25 nm
Compressed IR pulse length (FWHM)		0.87 ps	20 ps
Frequency conversion		263 nm (4ω)	1064, 532, or 355 nm (1, 2, 3ω)
Delivered energy		30 μJ	150 mJ (at 2ω)
Delivered spot size		1.2 mm diameter	36 μm rms
Delivered spot shape		Flattop	See Fig. 9

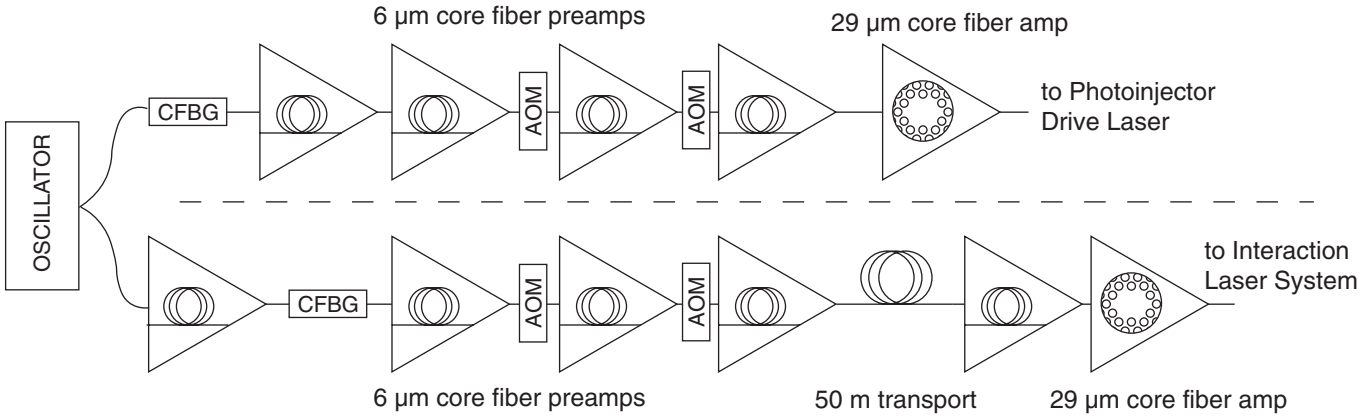

FIG. 2. Schematic diagram of the SLS architecture, showing the chirped fiber Bragg grating (CFBG), acousto-optic modulators (AOM), and the standard and photonic crystal fiber amplifier stages.

The ILS subsystem is similar to the PDL; it is fed by the same oscillator and uses similar fiber-based amplifiers but operates at 1064 nm, instead of the 1053 nm of the PDL.

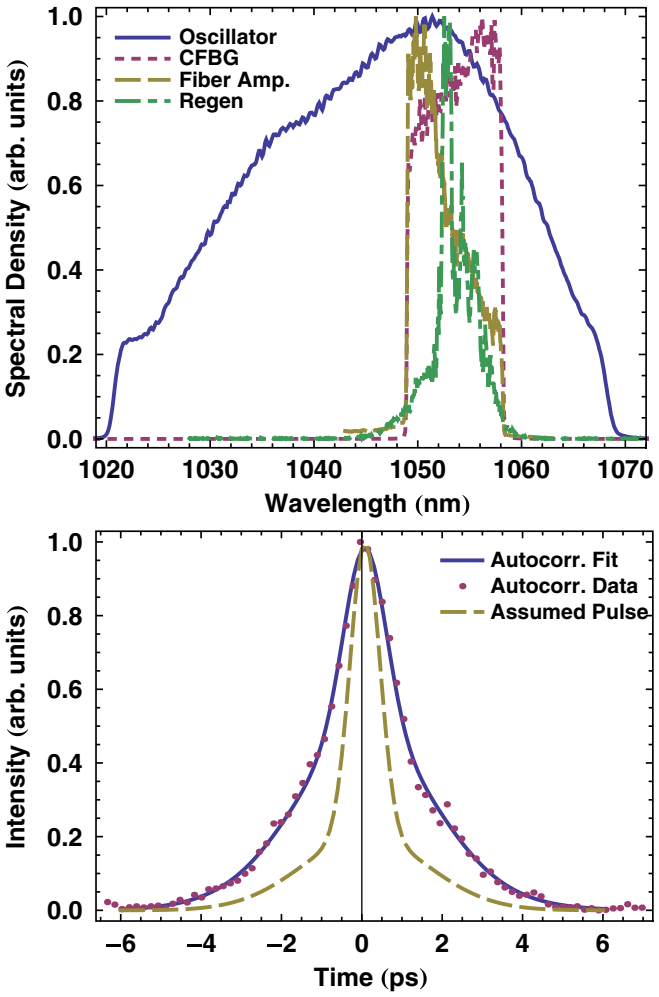

FIG. 3. (Color) Top: The spectrum of the PDL pulse at the oscillator, after the CFBG, after fiber amplification, and after regenerative amplification. Bottom: PDL compressed pulse autocorrelation data with a pulse-plus-pedestal fit.

The ILS's chirped fiber Bragg grating is double passed to stretch its pulses to 5 ns; the grating also intentionally narrows the spectrum to 0.8 nm. Double passing and the spectral narrowing bring the CFBG loss to 30 dB; consequently, one preamplifier is placed prior to the stretcher to ensure that sufficient signal remains after it to seed the following amps. The final fiber amplifier delivers 30 μJ pulses at 10 kHz.

Though the PDL and ILS chirped fiber Bragg gratings both stretch their respective pulses to the few-ns level, the ILS bandwidth is much narrower (0.8 nm vs 8 nm), giving it approximately 10 times the temporal dispersion. This led to two challenges. First, the errors in the relative delay of the different frequencies of the ILS pulse are proportionally larger than for the PDL pulse (an artifact of the grating manufacturing process). This error appears as a periodic ripple in the relative delay as a function of wavelength. Measurements [15] showed that the ILS ripple was on the order of 30 ps peak to peak at a period of 0.1 nm; nonlinear distortions in the final fiber amplifier exacerbated this ripple and limited the pulse energy from the fiber seed to 30 μJ.

The second effect of the larger temporal dispersion in the ILS stretcher was temporal jitter, Δt. This stemmed from uncontrolled temperature variations ΔT, according to the expression:

$$\frac{\Delta t}{\Delta T} = \left(\frac{1}{\lambda}\frac{d\lambda}{dT}\right)\lambda_0 D, \tag{1}$$

where λ_0 refers to the mean wavelength of the stretcher (1 μm) and D represents its temporal dispersion, typically expressed in ps/nm. The quantity in parentheses is the fractional change in center wavelength with temperature; for silica, this is roughly 9×10^{-6}/C. The dispersion of the ILS stretcher is 7100 ps/nm at 1064 nm, and so it generates a temporal drift of 68 ps/C. The ILS stretcher thus calls for temperature control to within ± 0.3°C. This was accomplished by enclosing the fiber in an insulating housing and heating it to 120°C, which also shifted the center

wavelength of the grating to lie within the gain bandwidth of the Nd:YAG rods that were used for amplification.

B. Photoinjector drive laser (PDL)

To minimize the contribution of space-charge effects on the electron beam emittance, our target laser pulse shape is a uniform-intensity cylinder of photons, based on previous simulations of our photoinjector [16]. The pulse provided by the fiber seed has to be shaped in both space (via aperturing) and time (via pulse stacking) to generate the desired profile. Furthermore, the energy delivered by the fiber seed is not sufficient to drive the photocathode directly given the quantum efficiency of the photocathode (1×10^{-4}) and desired 1 nC operating point.

The pulse energy is boosted by a regenerative amplifier based upon the design for those deployed in the preamplifier modules of the NIF [17]. The amplifier head consists of a Nd:phosphate glass (Schott LG770) rod that is end pumped by an 800 nm laser diode array homogenized by a hollow duct concentrator. The amplifier was designed to operate at 10 Hz with an 18 ns round-trip time. The diode pump power and number of round-trips were adjusted to yield 1.5 mJ output pulses at peak buildup for maximum energy stability. A Pockels cell enabled Q-switched cavity-dumped operation.

After the regenerative amplifier, the pulse is recompressed with a transmission efficiency of 66%. The compressor grating is a 1740 l/mm dielectric grating at an incidence angle of 75°, with a translatable horizontal roof mirror to set the effective grating separation and a vertical roof mirror to offset the beam for extraction at the compressor exit. The spectrum after the compressor is shown in Fig. 3 (top). The bandwidth of the pulse has been reduced due to gain narrowing in the regenerative amplifier, and now only has enough bandwidth to support ≥ 0.6 ps FWHM pulse widths. An autocorrelation measurement of the compressed pulse is shown in Fig. 3 (bottom), and is consistent with a 0.87 ps FWHM pulse with a 3.6 ps pedestal containing about 20% of the pulse energy. Following the compressor the pulse is frequency doubled to 527 nm with a 1.0 mm thick β-barium borate (BBO) crystal, then doubled again to 263 nm with a 0.45 mm thick BBO crystal, yielding a final energy of 100 μJ before pulse shaping.

We have approximated the necessary temporal shape by stacking several short pulses together to minimize the rise and fall times of the beam. The frequency-quadrupled pulse is fed into a hyper-Michelson pulse stacker [18], which splits the pulse into 16 replicas through a series of four beam splitters. By sequencing the beam splitters correctly [using the two outputs (one with variable delay) of the first as two inputs to the second, etc.], rotating the polarization of one of the two final outputs with a wave plate, then combining the two outputs with a polarizer, no laser energy is wasted. Choosing the delays correctly allows adjacent pulses to have crossed polarizations, minimizing interference between the pulses which could lead to significant longitudinal ripple on the delivered pulse. Because we are illuminating the photocathode nearly on axis, the polarization of the laser light is not significant.

The resulting temporal profile was measured in two ways. First, the residual IR light (first harmonic or 1ω) is mixed with the frequency-quadrupled (fourth harmonic or 4ω) UV light in a BBO crystal. Nonlinear mixing of the 1ω and 4ω light in the crystal generates third harmonic light (3ω) by difference frequency generation. By varying the arrival time of the IR pulse relative to the UV pulse, a cross correlation of the two pulses is found and can be used to infer the UV pulse length. The pulses were measured in groups of four so they could be individually resolved in the cross correlation, and the results are shown by the bottom traces of Fig. 4 (top). The Gaussian width of the individual pulses is $\sigma = 0.83$ ps. This is consistent with an initial IR pulse width of $\sigma_{\mathrm{ir}} = 0.74$ ps and a UV pulse width of $\sigma_{\mathrm{uv}} = 0.37$ ps.

The second measure of the temporal profile came from recording each of the individual pulse energies at the output of the hyper-Michelson stacker, which is done by selectively blocking various delay arms. Using this set of energies, coupled with the width measured in the cross correlation, to define Gaussian pulses to sum, the expected pulse shape is shown in the upper plot of Fig. 4 (top-dashed line). Scaling the cross-correlation measurements based on the measured energy of the largest pulse in each group, then summing those four plots, we obtain the curve shown in the upper plot of Fig. 4 (top-solid line). The deviation from the target flattopped shape is due to the uneven splitting ratio of the beam splitters used—measurement of the transmission of each of the splitters predicts the energy distribution observed. This issue will be addressed in future designs.

To produce the required flattop transverse beam shape, the output of the hyper-Michelson stacker is clipped by a 1.2 mm diameter aperture. Although this method has the disadvantage of discarding a significant amount of laser light, it has the advantages of being both simple to implement and easy to modify (to allow optimization of the electron emittance). The Gaussian beam size at the aperture is measured to be $\sigma_x = 0.61$ mm $\times$ $\sigma_y = 0.87$ mm, which means the 1.2 mm diameter aperture will pass only 28% of the laser energy. The aperture plane is relay imaged with a pair of 1 m focal length lenses, forming a 1:1 imaging telescope, to the cathode surface in the photoinjector. A small portion of the beam is picked off and sent to a camera sitting at an equivalent image plane (Fig. 4) and an energy meter. The energy delivered to the photocathode is adjusted to get the desired operating charge. Up to 30 μJ are available at the cathode, but a value of 17 μJ (with an rms energy jitter of 1 μJ) is typically used for normal operation.

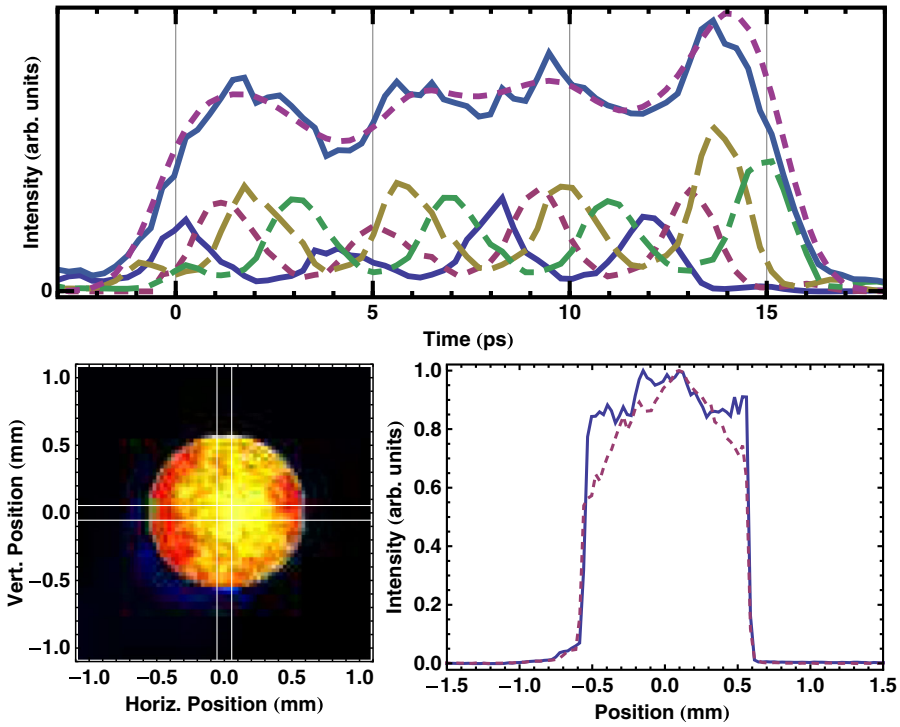

FIG. 4. (Color) Top: Cross correlation of PDL stacked UV pulse with residual IR. The bottom traces show the 16 individual pulses, and the upper traces show the sum of the cross correlations (solid curve) and the expected shape based on individually measured pulse energies (dashed curve) (see text). Bottom: The apertured PDL profile (left), and averaged lineouts within the boxed regions (right—solid: vertical, dashed: horizontal).

C. Interaction laser system (ILS)

The design specifications for the ILS were chosen to optimize the scattering process that is fundamental to the operation of the Compton source. The probability of an electron experiencing scattering processes, and the number of such processes it experiences, is proportional to the column density of the photon field along the direction of travel of the electron. To maximize the γ-ray flux, we want to maximize the column density, subject to two limiting factors. First, if the photon density becomes too high, nonlinear effects (multiple scattering events) start to dominate the scattering and significantly broaden the bandwidth of the source. To avoid this, we want to make the laser pulse as long as possible. Additionally, long pulses require less bandwidth in the laser spectrum, and laser bandwidth contributes linearly to γ-ray bandwidth [$E_\gamma \propto E_l$, see Eq. (3) below]. The second limiting factor is the length over which the laser and electron beams are focused. At distances z from the focal plane of the laser, the $1/e^2$ intensity radius w of the beam increases according to

$$w(z) = w_0\sqrt{1 + \left(\frac{z}{z_r}\right)^2} \qquad z_r = \frac{\pi w_0^2}{\lambda}, \tag{2}$$

where $w_0 = w(0)$ corresponds to the laser focal size and z_r is known as the Rayleigh range. This increase in beam size causes the photon density (and therefore the scattering rate) to drop. For $w_0 = 40$ μm and $\lambda = 532$ nm wavelength, z_r corresponds to an optimal interaction length of $\sim$30 ps. Having a pulse longer than this means part of the interaction will occur away from the focus, so more laser energy per scattered photon is required. We therefore selected a design pulse length of 10 ps to match that planned for the electron beam. To get pulse lengths on the order of 10 ps at $\lambda = 1$ μm wavelength requires a bandwidth 0.1 nm. This allows for the possibility of using commercial Nd:YAG technology, which has a gain bandwidth of $\Delta\lambda \approx 0.4$ nm, for amplification.

The ILS laser system starts with the fiber laser seed source discussed above, which supplies a 10 kHz train of 30 μJ pulses at 1064 nm with 1.3 nm bandwidth stretched to nominally 5 ns in the CFBG. This pulse duration is similar to that of commercial Q-switched Nd:YAG lasers. However, such commercial lasers are limited to a few longitudinal modes, as opposed to the relatively wide-spectrum chirped pulses that the fiber provides. The fiber amplification is split between preamplifiers that are colocated with the PDL fiber hardware and the photonic crystal fiber amplifier located in another room with the ILS bulk amplifier. The two systems are connected by a long (50 m) transport fiber. Following the fiber seed is a three-head Nd:YAG power amplifier and a hyperdispersion pulse compressor. The beam after the compressor, initially at 1064 nm, can then be frequency doubled or tripled using

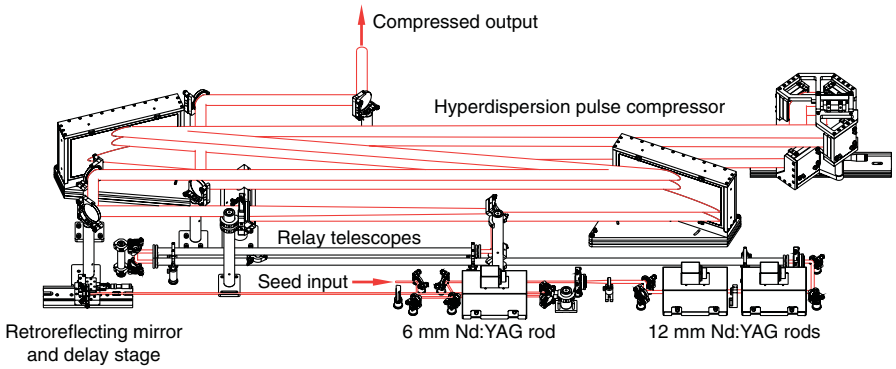

FIG. 5. (Color) Diagram showing the bulk amplifiers and compressor for the interaction laser system. The seed is sent though three Nd:YAG heads then relay imaged and upcollimated for injection into the hyperdispersion pulse compressor.

large aperture deuterated potassium dihydrogen phosphate, KD_2PO_4 (DKDP) crystals. The layout of the bulk amplifiers and the hyperdispersion compressor is shown in Fig. 5.

The custom Nd:YAG amplifier chain has been designed and built around three commercial heads from Continuum. The first laser head contains two side-by-side 6 mm diameter Nd:YAG rods pumped by a single flashlamp. The second and third laser heads each consist of a 12 mm diameter Nd:YAG rod. A pockels cell before the amplifier slices out a 10 Hz pulse train from the fiber seed. The pulses then double pass each of the 6 mm diameter rods and single pass each of the 12 mm diameter rods. An expanding telescope doubles the beam size before the 12 mm rods. The spatial beam profile is Gaussian and the fill factor in the rods (20%–25%) is kept small enough to minimize interference rings caused by beam clipping. Negative lenses placed after laser heads compensate for thermal focusing and a quartz half-wave rotator between the 12 mm rods partially compensates for thermal birefringence. An adjustable delay stage after the first pass through the 6 mm heads is used to control the relative timing between the laser pulses and the electron beam at the interaction point. The seed pulse energy is amplified to 1.2 J and the pulse bandwidth is gain narrowed from 1.3 nm FWHM in the seed pulse to 0.25 nm at the amplifier output.

For pulse compression, we use a novel hyperdispersion grating compressor. Chirped-pulse amplification in Nd:YAG with subnanometer bandwidths is impractical using traditional two-grating pulse compressors due to exceedingly large grating spacing (~ 25 m with 1740 grooves/mm gratings). We use a cascaded ''hyperdispersion'' architecture to provide the necessary temporal dispersion (7100 ps/nm) in a compact meter-scale compressor. Our design uses four multilayer dielectric (MLD) diffraction gratings in a double-pass configuration. The use of MLD gratings allows for high throughput efficiency in the compressor despite a total of eight grating reflections. The beam is incident at 3° off the Littrow angle on all of the 1740 g/mm gratings. The first grating angularly disperses the incident collimated beam, and the second grating is arranged antiparallel to the first and further disperses the beam. The third and fourth gratings are arranged parallel, respectively, to the second and first gratings to collimate the spatially chirped beam. To simplify multigrating alignment and reduce grating cost, we fold the beam path to reduce to two the total number of gratings. The chosen grating dimensions are 40×20 cm^2, determined by the total temporal chirp of the laser pulse and the damage fluence of the MLD gratings. Each grating sees four beam reflections at four different heights. To fold the beam, a six-mirror assembly (effectively three periscopes) adjusts the beam height between grating passes and spatially inverts the chirped beam along the direction of propagation.

Autocorrelation measurements of the compressed IR pulse duration are shown in Fig. 6 (top left). The autocorrelation has a narrow (28 ps) central lobe and a wide pedestal; the latter contains approximately 80% of the total energy. The width of the central lobe is consistent with a 20 ps FWHM pulse duration. The measured pulse spectrum recorded with a $f = 1.5$ m McPherson spectrometer shows an amplified bandwidth of 0.25 nm [Fig. 6 (top right)]. The oscillation in the spectrum with a 0.05 nm period is indicative of prepulses and postpulses spaced 75 ps apart. The poor temporal pulse compression we observed is caused by a periodic modulation in the CFBG dispersion discussed in Sec. I A. Although the longer main pulse width is larger than the 10 ps target, it is still smaller than z_r for the focal spot size and should not impact γ-ray production significantly. The fact that only 30% of the energy is contained in the main pulse will translate into a reduction of the scattered γ-ray flux.

Before delivery to the interaction point, the compressed IR beam can be frequency converted to attain appropriate energy ranges of the Compton generated γ-ray beam. The ILS can be reconfigured to provide either the fundamental or the 2nd or 3rd harmonic frequency. Frequency conversion is accomplished with large aperture DKDP crystals. 150 mJ of 2ω light ($\lambda = 532$ nm) is produced using a

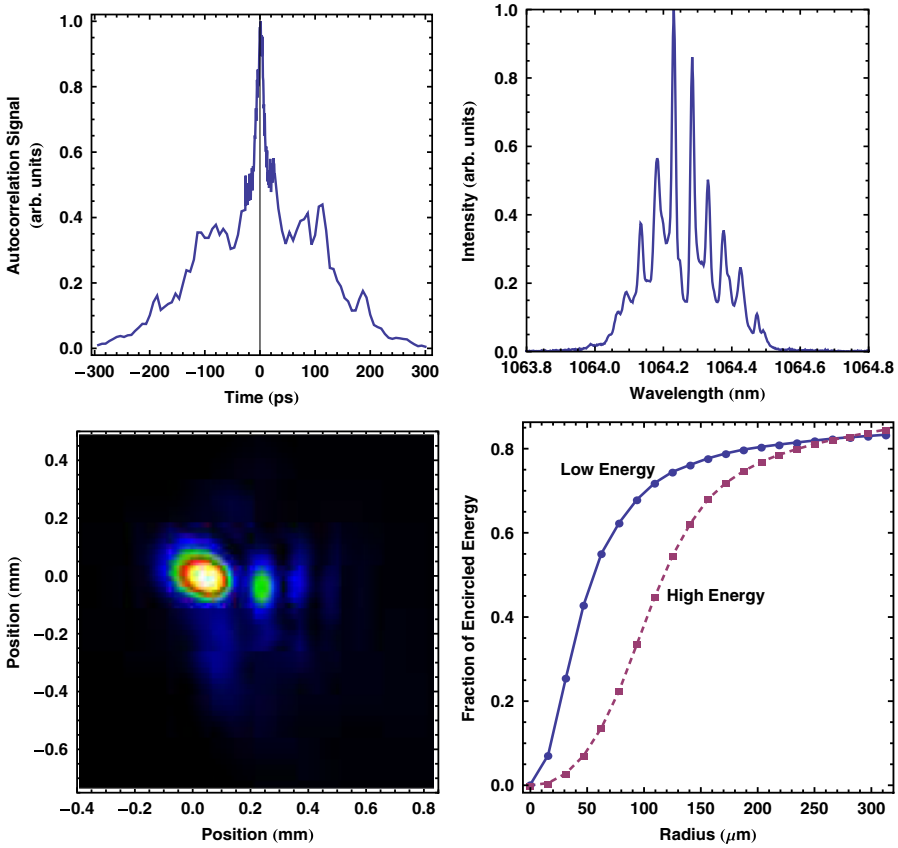

FIG. 6. (Color) Top left: Autocorrelation trace of the compressed ILS IR pulse. Approximately 20% of the energy is in the central peak. Top right: Spectrum of the compressed ILS IR pulse. Bottom left: Profile of the ILS focal spot after an $f = 2.4$ m lens. Bottom right: Fraction of total energy contained within an aperture of a given radius for low- and high-energy system output.

30×30 mm aperture, 6 mm thick DKDP crystal cut for type II doubling. At 3ω, 120 mJ of 355 nm light is generated using two 60×60 mm aperture DKDP crystals. The doubling crystal is cut for type I phase matching and the tripling crystal is cut for type II phase matching, producing up to 120 mJ of 3ω light. The typical energy jitter is 2% in the fundamental pulse, and 4% in the 2nd harmonic and 3rd harmonic.

The laser pulse is focused to the interaction point with an $f = 2.4$ m lens. Low order wave front aberrations result in a focused beam that is twice the diffraction limit. Additionally, several upstream optics, mainly laser rods and compressor mirrors, aperture the beam producing high frequency spatial modulation. At the beam focus, this results in a pedestal which contains a large fraction of the overall energy. The focal distribution of the 2ω light recorded with a 12-bit camera is shown in Fig. 6 (bottom left). Additional side lobes at the focus are indicative of beam clipping. In order to determine the generated γ-ray dose, an important figure of merit is the energy contained within the spot overlapped with the electron beam. Figure 6 (bottom right) shows the encircled energy contained within an aperture of radius R. For a high-energy (150 mJ) focused 532 nm beam, 30% of the total energy is contained within a 100 μm radius aperture.

The time duration of the 2ω signal was not measured directly. Computer simulations of the frequency doubling process, assuming a 1ω pulse which contains 30% of the total energy in the 20 ps central peak and the rest of the energy in a 600 ps wide pedestal, indicate that frequency conversion will slightly shorten the pulse length and suppress the pedestal due to the nonlinear nature of the process. After doubling, approximately 50% of the 2ω energy should be in a 16 ps central peak with the rest of the energy contained in the wide pedestal.

II. ELECTRON SYSTEMS

Precision electron beam generation requires that the laser arrival time at the photocathode be synchronized to within 1° of phase to the accelerating rf in the photoinjector cavity; thus, the two systems must be locked to the same clock. As mentioned above, the laser is locked to a 40.7785 MHz reference crystal oscillator, the 70th subharmonic of the 2.8545 GHz operating frequency of the accelerator. The laser photodiode signal, used to keep the laser locked to the master crystal and to generate the timing triggers for all the laser and accelerator systems, is also filtered to produce a sinusoidal rf signal that tracks the laser pulse train even if it drifts from the reference frequency.

This signal is fed into a phase-locked coaxial resonant oscillator which puts out S-band rf phase locked to the laser pulse train. The mW level rf power is distributed to a set of six modules consisting of a kW amplifier and pulsed klystron, producing 3–4 μs pulses of roughly 20 MW of peak rf power. These modules independently drive the photoinjector and the five separate accelerating sections, allowing independent phase and power control over each rf structure.

The T-REX injector is a 1.6 cell photocathode gun of the BNL/SLAC/UCLA/LLNL design [19]. There are, however, several key changes from previous designs [20]. Because on-axis laser injection is used, the 70° ports of the half cell were removed, making the half cell fully cylindrically symmetric. The full cell was also symmetrized to quadrupole moment by replacing the tuning plungers, which have been found to break down at high field and limit gun performance [21], with race-track shaped slots identical to the rf coupling slot.

Another significant change to the gun design was to increase the frequency separation of the 0 and π modes. This modification was first implemented at SLAC in order to minimize the excitation of 0-mode fields which were found to have a detrimental effect on the beam emittance and energy spread [22]. The mode separation of the T-REX gun was increased to 12.3 MHz. PARMELA simulations were performed and indicate that the effect of the 0-mode is negligible at the larger mode separation, in agreement with the results of [22].

The photoinjector cathode is a 1 cm diameter, 2 μm thick layer of Mg sputter coated onto the copper backplane of the half-cell cavity. When powered, the peak on-axis field in the gun reaches 120 MV/m. When illuminated with 17 μJ of light from the PDL, an 800 pC electron bunch is produced with a quantum efficiency (QE) of 1×10^{-4} at 30° injection phase. No efforts were made to improve the QE or the QE uniformity through *in situ* cleaning methods [23,24]. At the entrance to the linac, the beam energy is 5.5 MeV with a normalized emittance of $\epsilon_{n,xy} = 1.8$ mm mrad measured with a pepper-pot mask.

The beam generated by the photoinjector is then coupled into the linear accelerator at LLNL [25]. Originally designed for high-current beams used for neutron production, some upgrades to the system were required. An additional 8 ft SLAC-type S-band disk-loaded traveling-wave linac section was added to the preexisting architecture to allow us to reach an end point energy of 120 MeV, bringing the total number of identical accelerating sections up to five. The beam focusing solenoids on each section were not used due to concerns about the alignment of the magnetic and rf axis and the potential for emittance growth from quadrupole field errors in the presence of a solenoidal field [26]. Instead, quadrupole doublets or triplets were inserted between the sections to control the beam growth.

The emittance of the electron beam was measured at the end of the accelerator using a quadrupole scan, and yielded a normalized rms emittance of $\epsilon_{n,x} = 4$, $\epsilon_{n,y} = 8$ mm mrad. Based on the beam energy, charge, and drift length in the system, space-charge forces had a negligible effect on this measurement [27]. The most likely source of the emittance growth is the asymmetric waveguide feed on the accelerator sections, a well-known issue for the SLAC section design [26,28]. A summary of the measured electron beam parameters is presented in Table II.

TABLE II. Laser and electron beam parameters at the interaction point for nominal operation.

Laser	
Repetition rate	10 Hz
Wavelength	532 nm
Bandwidth (FWHM)	0.1 nm
Total pulse energy[a]	150 mJ
Pulse length (FWHM)[b]	16 ps
rms spot size	34×38 μm
Electrons	
Repetition rate	10 Hz
Energy	116 MeV
rms energy spread	0.2%
Beam charge	800 pC
Bunch length (FWHM)	16 ps
rms spot size	23×42 μm
rms normalized emittance	4×8 mm mrad

[a]Energy in 100 μm aperture and 16 ps FWHM main pulse: 22 mJ. See text for details.
[b]Based on models of frequency conversion.

III. INTERACTION

Assuming a plane wave with wavelength λ impinging upon an electron traveling with relativistic factor γ at a 180° interaction angle, performing the Lorentz transformation to the electron rest frame, Compton scattering the laser off the electron, then transforming back into the lab frame, yields the scattered photon energy as a function of angle θ relative to the electron beam direction (neglecting nonlinear effects resulting from high laser photon densities):

$$E_\gamma(\theta) = \frac{4\gamma_e^2}{1 + \gamma_e^2\theta^2 + 4\gamma_e \frac{\lambda_c}{\lambda}} E_l, \tag{3}$$

where $\lambda_c = \frac{h}{mc} = 2.426 \times 10^{-12}$ m is the Compton wavelength, γ_e is the Lorentz factor of the electron, and $E_l = \frac{hc}{\lambda}$ is the laser photon energy. Simplifying assumptions of a highly relativistic beam ($\beta \approx 1$) and a small angle of interest for observation ($\theta \ll 1$) have been made. The latter assumption is useful for a highly relativistic beam because most of the light is scattered into a narrow forward

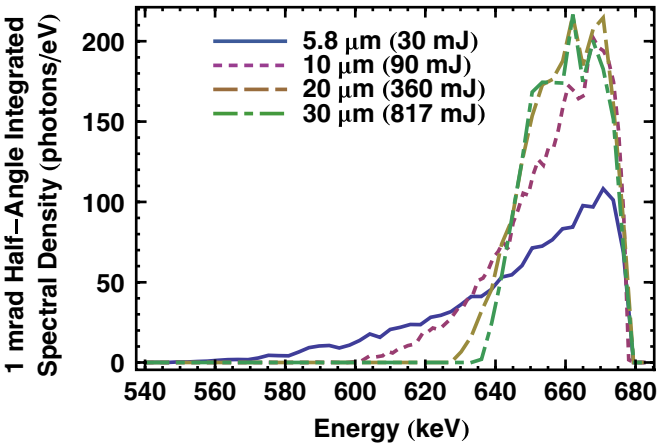

FIG. 7. (Color) Plot of the predicted integrated spectrum of the γ-ray source as a function of electron rms spot size. Smaller sizes show broadening due to the large angular distribution of the electron beam.

cone due to the Lorentz transformation. The scattering process allows a 532 nm laser and an electron beam with a kinetic energy of 120 MeV colliding at $\phi = 180°$ to produce a 516 keV photon beam with a relatively narrow bandwidth that is determined by the degree of collimation of the beam, the intrinsic angular spread in the laser and electron bunches at the interaction point, and the energy spread of the electrons and photons themselves. Optimizing the gamma-ray performance requires optimizing these parameters at the interaction point.

A. Interaction architecture

The interaction architecture was driven by the requirement of having a 180° interaction geometry to maximize the overlap between the laser and electron bunch (thereby maximizing γ-ray flux) and the desired spot size for the interaction. The interaction spot size was chosen based on a study of the spectrum of γ rays generated by different electron focus sizes. PARMELA [29] simulations of the full accelerator system, including a quadrupole triplet to focus the final beam, and assuming the optimal gun parameters as discussed in [16], were run to produce electron distributions of different focal sizes. These distributions were then fed into the scattering code [30] to calculate the γ-ray spectra over a 1 mrad half-angle cone (the expected size of the largest aperture we would use to collimate the beam), and the results are shown in Fig. 7. In this figure the fine structure on the spectra is an artifact of the undersampling of the electron phase space resulting from the number of particles (50 000) used in the PARMELA simulation. The laser spot size was chosen to match the electron spot size, and the laser energy set to keep the square of the normalized vector potential of the lasers electromagnetic field, which is proportional to photon density, at a value of $a_0^2 = 0.1\%$ to avoid spectrum-broadening nonlinearities in the scattering (which the code does not include). For small spot sizes, a significant broadening of the spectrum is seen, a result of the increased angular distribution that a fixed emittance requires of smaller focal spots. Once an rms size of $\sigma_{x,y} = 20$ μm is reached, however, the bandwidth is limited mostly by the inherent single-electron bandwidth of the included solid angle, which for $\gamma_e = 220$ is 4.6%. Any spots larger than 20 μm require significantly more laser energy to keep the photon density the same, but do not provide any increase in the number of photons per eV that are generated. In fact, since the spot size is increasing, the overall spectral brightness of the source goes down. Therefore a $\sigma_{x,y} = 20$ μm spot was chosen as the design point.

This spot size requirement implies for the laser that the required f number is $f/\# \equiv \frac{F}{d} = \frac{\pi w_0}{2\lambda} = \frac{\pi \sigma_x}{\lambda} \geq 60$ for $\lambda \leq 1.064$ μm, where F is the focal length of the beam and d is the beam diameter at the focusing element, is needed for the beam, which allows for a long focal length. Thus, the interaction geometry shown in Fig. 8 is the simplest choice. The electron beam is brought to a focus by a pair of quadrupole triplets. The first triplet is designed to match the spot size and emittance at the end of the acceleration sections to that needed to produce the proper focus. Then a high-gradient (up to 15 T/m) quadrupole triplet brings the spot size down to the desired spot size. This system is designed to get beams with a normalized emittance up to 5 mm mrad to a 20 μm focus 25 cm past the end of the last magnet. After the interaction, the electron beam is bent off the main axis by a 20° dipole magnet which also serves as an electron energy diagnostic. A third quadrupole triplet

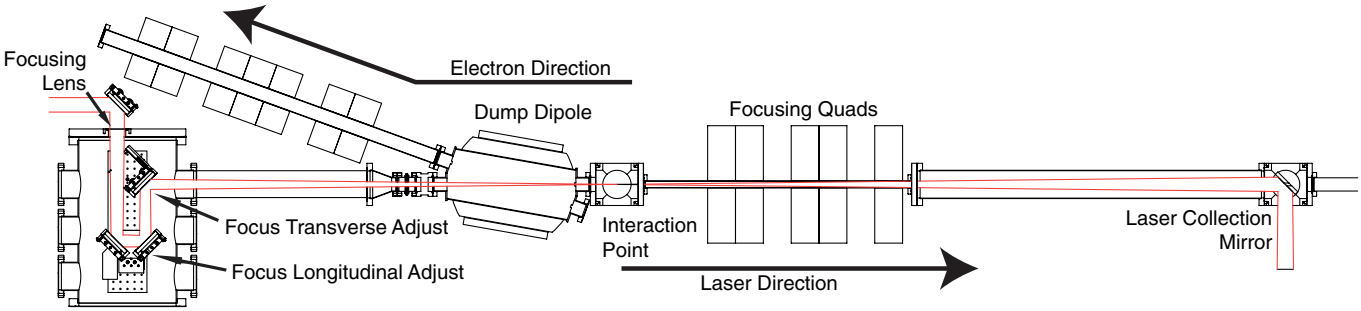

FIG. 8. (Color) Layout of the T-REX interaction region.

then captures the expanded electron beam and transports it to a well-shielded beam dump.

Meanwhile, the laser is focused by a $f = 2.4$ m lens which also serves as the window into the linac vacuum system. A pair of mirrors on a translation stage allow the position of the focus to be moved longitudinally about the interaction point, and a final motorized turning mirror allows the transverse positioning of the laser focus. Coupling that with a translation stage before the focusing lens to allow tweaking of the time of arrival of the laser, the system has 4D adjustment to get the laser to hit the electron beam at the interaction point.

To collect the residual laser light, an additional mirror is be placed in the linac beam line. To allow the electron beam to pass, it has a 1 cm hole in its center. In order to keep laser light from leaking through the hole in the mirror and potentially damaging the accelerator structure, a 1 cm obscuration is placed in the beam a distance of $2f$ before the focusing lens, which will cause an image of the obscuration a distance $2f$ after that lens, or f after the interaction point, which is where the extraction mirror is placed. The back of this mirror was silvered to allow optical transition radiation (OTR) imaging of the electron beam position on the back side to facilitate alignment of the beam through the aperture in the optic. Simulations of the modified laser profile focusing and scattering from the electron beam show that the shadow in the center of the laser before focusing does not affect electron production at the interaction point. With this scheme, the laser energy can be collected either for diagnostics or for recirculation of the unused photons [31]. Although demonstrated in the 3ω runs, the optic was removed when the system was switched to 1ω operation and not reinstalled for further experiments, since the collected beam was not being used.

To establish the relative alignment of the laser and electron beams, an optically polished 8 mm nickel cube, attached to a two-axis translation stage, is located at the interaction point (following the same scheme described in detail in [32]). Oriented with the vertical faces at 45° to the electron-laser beam line, the laser (significantly attenuated in energy by mistiming the flashlamp firing and turning down the fiber pump diodes) will reflect off the surface and the electron beam will generate OTR light at an angle corresponding to the reflection angle. This light is imaged with a camera to ensure the beams are aligned vertically, and the overlap horizontally can be determined by seeing the beams meet at the edge [Fig. 9 (top)]. The light is also imaged onto an Imacon 500 Series streak camera (maximum resolution 2 ps) to allow the adjustment of the laser delay to get the correct temporal overlap [Fig. 9 (bottom)]. The timing of the interaction laser pulse is adjusted coarsely by selecting the appropriate pulse from the 40.7785 MHz oscillator to amplify in the ILS. The oscillator period gives 24 ns steps. To get 1 ns resolution, the length of fiber in the ILS transport line (between the fiber

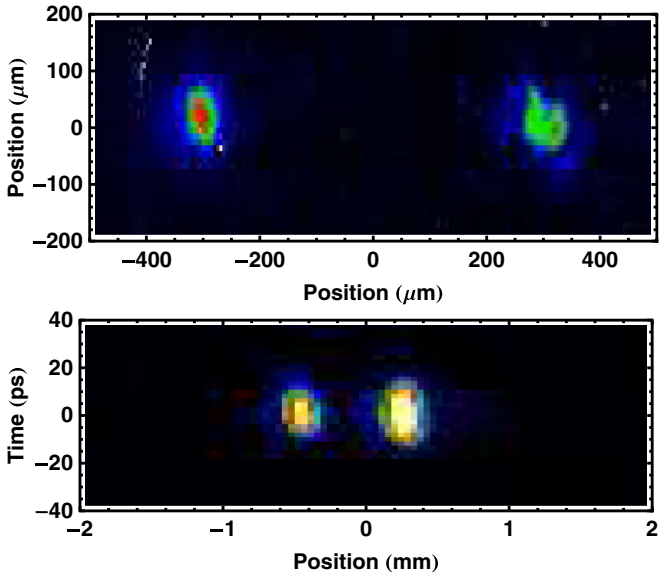

FIG. 9. (Color) Images of the laser and electron beams at the interaction point. Top: Beam spatial profile on alignment cube (electrons left, laser right). Bottom: Streak camera image of the two beams on the alignment cube (laser left, electrons right).

amplifiers colocated with the PDL and the ILS bulk amplifiers) is adjusted. The final 10 ps resolution is achieved by adjusting the delay stage holding the retroreflecting mirror in the middle of the 6 mm diameter rod assembly in the amplifier chain of the ILS (shown in Fig. 5).

Measurement of the two beams on the alignment cube shown in Fig. 9 yield a Gaussian fit with an rms spot size of 34×38 μm for the laser focus and 23×42 μm for the electron focus. The streak camera images provide evidence that the pulses are on the order of 10 ps in length. Analysis of several consecutive electron beam images at the cube provides a measurement of the beam centering jitter, which is on the order of 20 μm rms. Performing a similar analysis on an image of the beam after the dipole magnet allows an estimate of the pointing jitter of the beam. We observe an angular jitter of 1.2 mrad in the x direction (the direction of the dipole deflection) and 0.6 mrad in the y direction. In the x direction the angular jitter is a combination of both beam pointing jitter and shot-to-shot energy jitter. Based on jitter measurements before the final-focusing quadrupoles and a matrix analysis of the focal region transport, the energy jitter is a minimal contribution to the observed jitter. This angular jitter is significant for the γ-ray production because of the dependence of the scattered photon energy on the observation angle. Integrating over numerous shots, a large pointing jitter behaves identically to a large emittance in terms of the generated photon bandwidth. The position jitter has a direct impact on the total scattered γ-ray flux, and is thus essential to minimize.

A summary of the laser and electron beam parameters delivered to the interaction point are presented in Table II

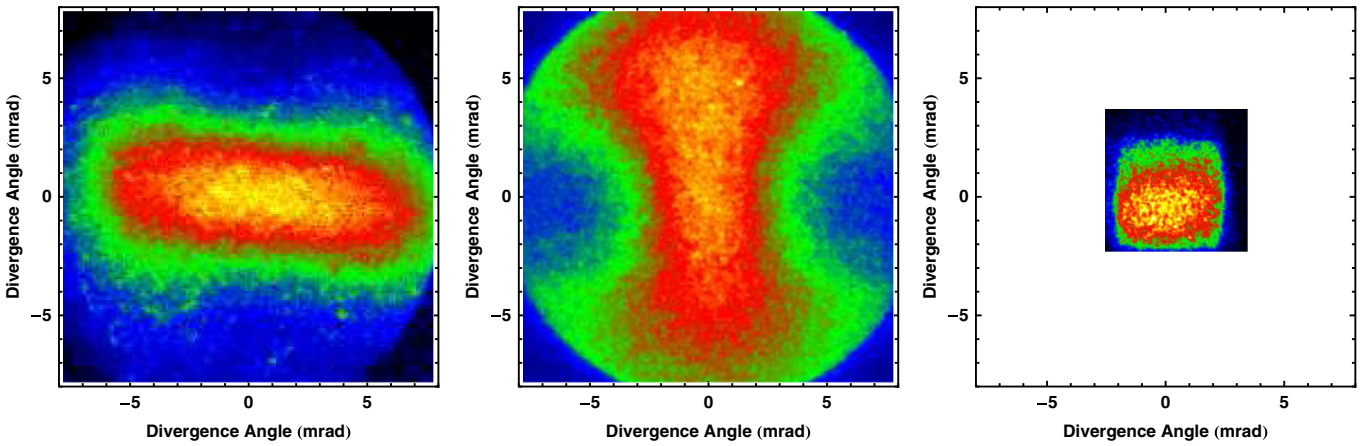

FIG. 10. (Color) γ-ray beam profiles from scintillator-coupled CCD cameras for the three laser frequencies. The beam energies are: left—295 keV (128.4 MeV + 1ω), center—466 keV (114 MeV + 2ω), and right—906 keV (130 MeV + 3ω).

B. γ-ray generation

Gamma rays were generated in three different laser configurations: 1ω where the ILS pulse was used without any frequency conversion ($\lambda_{1\omega} = 1064$ nm and $E_{\gamma,1\omega} \approx 225$ keV), 2ω where the laser is frequency doubled ($\lambda_{2\omega} = 532$ nm and $E_{\gamma,2\omega} \approx 450$ keV), and 3ω where the laser is frequency tripled ($\lambda_{3\omega} = 355$ nm and $E_{\gamma,3\omega} \approx 675$ keV—all assuming $\gamma \approx 220$ for the electron beam, a typical number). Two different charge coupled device (CCD) cameras were used to detect the produced γ rays. The first, used for the 1ω scattering, was a Princeton Instruments 16-bit, 1340 × 1300-pixel, 2.54 mm × 2.54 mm CCD coupled via a 3:1 demagnifying fiber optic bundle to a 145-μm thick CsI(Tl) scintillator. The second, used for the 2ω and 3ω measurements, is a 16-bit, 1024 × 1024-pixel, 13.3 mm × 13.3 mm, gated and intensified CCD Andor iStar camera. For the 3ω scattering, this system was fiber-optically coupled to a 150 μm CsI(Tl) scintillator with no demagnification of the beam (thus only showing a portion of the profile). For the 2ω runs, a fiber taper with a 3:1 demagnification coupled the camera to the scintillator, giving a 4 cm × 4 cm observation area.

Figure 10 shows the images from the cameras for the three energies. The 1ω (left) and 2ω (center) images show a hard round aperture which is the steel flange holding the 300 μm Be plate used as a vacuum window. The 3ω image (right) shows a 1 cm square aperture in a lead brick. This aperture was used to give a discernible profile to the beam because the beam overfilled the observation window of the camera. The distorted shape is a result of the $\sin^2$ distribution of the dipole scattering in the electron rest frame. In the electron rest frame, the null points of the radiation pattern are at 90° to the beam line axis, along the direction of the laser polarization. However, the Lorentz transformation of angles when moving to the lab frame gives

$$\cos\theta = \frac{\cos\theta' + \beta}{1 + \beta\cos\theta'}, \tag{4}$$

so when $\theta' = 90°$ and $\beta = \sqrt{1 - \frac{1}{\gamma^2}}$ with $\gamma = 220$, we find $\theta = 4.5$ mrad. In the 1ω case, the laser is polarized vertically, leaving the nulls of the radiation pattern aligned vertically as well. As a result of the frequency doubling process, the laser is polarized horizontally in the 2ω case with a consequent horizontal alignment of the nulls.

IV. CONCLUSIONS

We have demonstrated a tunable MEGa-ray source using the principle of Compton scattering and generated energies ranging from 75 keV to 0.9 MeV. A thorough measurement of the γ-ray beam parameters (summarized in Table III), demonstrating a peak spectral brightness of 1.5×10^{15} photons/mm^2/mrad^2/s/0.1% bandwidth (BW) and a detected flux of 1.6×10^5 photons/shot is presented in [33], along with experiments conducted with the source. The successful operation of this system lays the groundwork for the construction of a full-energy (~ 2 MeV) MEGa-ray source.

This system underperformed in two main respects. While the newly designed and installed photoinjector operated as planned, sustaining a 120 MV/m gradient using a sputtered Mg photocathode, and delivering a 1.8 mm mrad emittance at 5.5 MeV, the emittance was significantly degraded by the time it reached the interaction point. This was because we used accelerating sections and an rf power system which were originally designed to accelerate

TABLE III. Gamma source performance parameters.

Photons per interaction	1.6×10^5
Peak (on-axis) energy	478 keV
rms energy spread	12%
Repetition rate	10 Hz
Peak (on-axis) brightness	1.5×10^{15} $\frac{\text{photons}}{\text{mm}^2\ \text{mrad}^2\ \text{s}\ 0.1\%\ \text{BW}}$
Inferred rms spot size	$\sim$36 μm
Beam divergence	10 × 6 mrad

a very high-current thermionic beam 40 years ago. Known field errors in the section design were not corrected leading to the emittance growth and subsequent broadening of the gamma-ray spectrum, and instability in the rf system resulted in large jitter and drift of the electron beam (both in position and size) at the focal spot, reducing the average measured flux. The second was a result of quality control issues on the ILS fiber stretcher and bulk compressor optics, which resulted in poor compression and focusability of the laser pulse. Because of these effects, only about $1/6$ of the total laser energy was available at the interaction point, and only 24% conversion efficiency to the second harmonic. Fixing these two issues could allow for a system with a peak spectral brightness 10^3 higher than that demonstrated here.

ACKNOWLEDGMENTS

We would like to thank John Heebner, Chris Ebbers, Andy Bayramian, and Scott Fochs for their help in the rapid assembly of the regenerative amplifier and ILS, Jay Dawson for his help in diagnosing PDL recompression efforts, Igor Jovanovic for his work on the initial stages of the laser design, and Gerry Anderson, Bob Berry, and Scott Fisher for assembly and operation of the linac systems. This work was performed under the auspices of the U.S. Department of Energy by Lawrence Livermore National Laboratory under Contract No. DE-AC52-07NA27344.

[1] A. H. Chin, R. W. Schoenlein, T. E. Glover, P. Balling, W. P. Leemans, and C. V. Shank, Phys. Rev. Lett. **83**, 336 (1999).
[2] H. R. Weller, M. W. Ahmed, H. Gao, W. Tornow, Y. K. Wu, M. Gai, and R. Miskimen, Prog. Part. Nucl. Phys. **62**, 257 (2009).
[3] E. C. Schreiber *et al.*, Phys. Rev. C **61**, 061604 (2000).
[4] C. Thorn, G. Giordano, O. Kistner, G. Matone, A. Sandorfi, C. Schaerf, and C. Whisnant, Nucl. Instrum. Methods Phys. Res., Sect. A **285**, 447 (1989).
[5] O. Bartalini *et al.*, Eur. Phys. J. A **26**, 399 (2005).
[6] T. Nakano *et al.*, Nucl. Phys. **A684**, 71 (2001).
[7] M. Sumihama *et al.*, Phys. Rev. C **73**, 035214 (2006).
[8] F. E. Carroll, M. H. Mendenhall, R. H. Traeger, C. Brau, and J. W. Waters, Am. J. Roentgenol. **181**, 1197 (2003).
[9] F. V. Hartemann, W. J. Brown, D. J. Gibson, S. G. Anderson, A. M. Tremaine, P. T. Springer, A. J. Wootton, E. P. Hartouni, and C. P. J. Barty, Phys. Rev. ST Accel. Beams **8**, 100702 (2005).
[10] W. Bertozzi and R. J. Ledoux, Nucl. Instrum. Methods Phys. Res., Sect. B **241**, 820 (2005).
[11] J. Pruet, D. P. McNabb, C. A. Hagmann, F. V. Hartemann, and C. P. J. Barty, J. Appl. Phys. **99**, 123102 (2006).
[12] F. Albert *et al.*, Opt. Lett. **35**, 354 (2010).
[13] J. W. Dawson, M. J. Messerly, H. H. Phan, J. K. Crane, R. J. Beach, C. W. Siders, and C. P. J. Barty, J. Sel. Top. Quant. Elect. **15**, 207 (2009).
[14] M. Durkin, M. Ibsen, M. J. Cole, and R. I. Laming, Electron. Lett. **33**, 1891 (1997).
[15] B. Costa, D. Mazzoni, M. Puleo, and E. Vezzoni, IEEE J. Quantum Electron. **18**, 1509 (1982).
[16] D. J. Gibson, S. G. Anderson, F. V. Hartemann, C. W. Siders, A. M. Tremaine, and C. P. J. Barty, in *Advanced Accelerator Concepts: 12th Workshop*, edited by M. Conde and C. Eyberger, AIP Conf. Proc. No. 877 (American Institute of Physics, Woodbury, NY, 2006), pp. 602–608.
[17] M. Bowers, S. Burkhart, S. Cohen, G. Erbert, J. Heebner, M. Hermann, and D. Jedlovec, Proc. SPIE Int. Soc. Opt. Eng. **6451**, 64511M (2007).
[18] C. W. Siders, J. L. W. Siders, A. J. Taylor, S.-G. Park, and A. M. Weiner, Appl. Opt. **37**, 5302 (1998).
[19] D. T. Palmer, Ph.D. thesis, Stanford University [SLAC Technical Report SLAC-R-500, 1998].
[20] A. Fukasawa, H. Badakov, B. D. O'Shea, E. Hemsing, J. B. Rosenzweig, and S. G. Anderson, in *Proceedings of the 2007 Particle Accelerator Conference, Albuquerque, New Mexico* (IEEE, Albuquerque, New Mexico, 2007), pp. 1260–1263.
[21] A. M. Cook, J. B. Rosenzweig, M. Dunning, P. Frigola, and K. Serratto, in *The Physics and Applications of High-Brightness Electron Beams: Proceedings of the 46th Workshop of the INFN ELOISATRON Project*, edited by L. Palumo, J. Rosenzweig, and L. Serafini (World Scientific, Singapore, 2005), pp. 353–364.
[22] C. Limborg, Z. Li, L. Xiao, J. Schmerge, D. Dowell, S. Gierman, E. Bong, and S. Gilevich, Stanford Linear Accelerator Center Technical Report No. LCLS-TN-05-3, 2005.
[23] X. J. Wang, M. Babzien, R. Malone, and Z. Wu, in *Proceedings of the 21st International Linac Conference, Gyeongju, Korea, 2002* (Pohang Accelerator Laboratory, Pohang, Korea, 2002), pp. 142–144.
[24] D. H. Dowell, F. K. King, R. E. Kirby, and J. F. Schmerge, Phys. Rev. ST Accel. Beams **9**, 063502 (2006).
[25] S. C. Fultz, C. L. Whitten, and W. J. Gallagher, IEEE Trans. Nucl. Sci. **18**, 533 (1971).
[26] D. H. Dowell, L. Bentson, R. F. Boyce, S. M. Gierman, J. Hodgson, Z. Li, C. Limborg-Deprey, J. Schmerge, L. Xiao, and N. Yu, in Proceedings of the 2004 FEL Conference, Trieste, Italy, pp. 538–541.
[27] S. G. Anderson, J. B. Rosenzweig, G. P. LeSage, and J. K. Crane, Phys. Rev. ST Accel. Beams **5**, 014201 (2002).
[28] R. B. Neal, edited by *The Stanford Two-Mile Accelerator* (W. A. Benjamin, New York, 1968).
[29] L. Young and J. Billen, Los Alamos National Laboratory Technical Report No. LA-UR-96-1835, 1996.
[30] W. J. Brown *et al.*, Phys. Rev. ST Accel. Beams **7**, 060702 (2004).
[31] I. Jovanovic, M. Shverdin, D. Gibson, and C. Brown, Proc. SPIE Int. Soc. Opt. Eng. **6881**, 68810F (2008).
[32] D. J. Gibson *et al.*, Phys. Plasmas **11**, 2857 (2004).
[33] F. Albert *et al.*, following article, Phys. Rev. ST Accel. Beams 13, 070704 (2010).